

Experimental Evaluation of Impulsive Ultrasonic Intra-Body Communications for Implantable Biomedical Devices

G. Enrico Santagati and Tommaso Melodia

Abstract—Biomedical systems of miniaturized implantable sensors and actuators interconnected in an intra-body area network could enable revolutionary clinical applications. Given the well-understood limitations of radio frequency (RF) propagation in the human body, in our previous work we investigated the use of ultrasonic waves as an alternative physical carrier of information, and proposed Ultrasonic WideBand (UsWB), an ultrasonic multipath-resilient integrated physical and medium access control (MAC) layer protocol. In this paper, we discuss the design and implementation of a software-defined testbed architecture for ultrasonic intra-body area networks, and propose the first experimental demonstration of the feasibility of ultrasonic communications in tissue mimicking materials. We first discuss in detail our FPGA-based prototype implementation of UsWB. We then demonstrate how the prototype can flexibly trade performance off for power consumption, and achieve, for bit error rates (BER) no higher than 10^{-6} , either (i) high-data rate transmissions up to 700 kbit/s at a transmit power of -14 dBm ($\approx 40 \mu\text{W}$), or (ii) low-data rate and lower-power transmissions down to -21 dBm ($\approx 8 \mu\text{W}$) at 70 kbit/s. We demonstrate that the UsWB MAC protocol allows multiple transmitter-receiver pairs to coexist and dynamically adapt the transmission rate according to channel and interference conditions to maximize throughput while satisfying predefined reliability constraints. We also show how UsWB can be used to enable a video monitoring medical application for implantable devices. Finally, we propose (and validate through experiments) a statistical model of small-scale fading for the ultrasonic intra-body channel.

Index Terms—body area networks, body sensor networks, implantable medical devices, Internet of Medical Things, ultrasonic communications and networking, acoustic communications and networking

I. INTRODUCTION

Biomedical systems of implanted or wearable miniaturized sensors and actuators wirelessly interconnected into an intra-body area network could enable revolutionary healthcare and clinical applications [2]. For example, remote cardiac rhythm monitors could detect cardiovascular malfunctions and trigger preemptive measures to mitigate their effects. Continuous glucose monitoring in diabetic patients could enable reactive administration of insulin through under-skin miniaturized drug deliverers. Camera-equipped implantable sensors could enable continuous remote monitoring of internal body organs and systems. Pill-sized ingestible cameras (already available) can monitor the gastrointestinal tract and avoid intrusive

examination techniques such as endoscopy. Large amounts of physiological data captured by implantable sensors could also be forwarded to an out-of-body gateway such as a smartphone or a smartwatch, and be made available to physicians and patients through the Internet. Pressure sensors implanted in the eye could detect high intra-ocular pressure (IOP) for early diagnosis and treatment of glaucoma to prevent vision loss, while monitoring of bone-growth in young diabetes patients could help prevent and treat osteoporosis. At an even smaller scale, wirelessly controlled nanorobots could detect and eliminate malicious agents and cells inside biological tissues, e.g., viruses and cancer cells, enabling less invasive and less aggressive treatments. Moreover, networked devices could be used for organ, nervous track, or tissue replacements, i.e., bio-hybrid implants.

As of today, existing wireless medical implants [3], [4] are connected through radio frequency (RF) electromagnetic waves. RF-based solutions tend to almost-blindly scale down traditional commercial wireless technologies (e.g., Wi-Fi, Bluetooth) to the intra-body environment, with little or no attention to the peculiar characteristics and safety requirements of the human body. We contend that this may not be the right approach. The human body is in fact composed (up to 65%) of water, a medium that absorbs RF electromagnetic waves significantly. As a consequence, RF waves need to be transmitted at higher power, which reduces the lifetime (or equivalently, increases the size) of the batteries of the implants. In addition, while the medical community is divided on the risks caused by continuous exposure of human tissues to RF radiations, the World Health Organization classifies RF waves as “possibly carcinogenic to humans” [5]. Moreover, RF-based wireless body networks may be affected by interference from other wireless systems. Finally, RF communications can be easily jammed through artificially generated interference, or eavesdropped. This raises major privacy and security red flags, and a risk for the patient.

Given these limitations, in [6], [7], [8] we proposed and investigated the use of ultrasonic waves as an alternative carrier of information in human tissues. Ultrasonic waves are acoustic waves with frequency higher than the upper threshold for human hearing (nominally 20 kHz). Acoustic waves have found application in underwater communications [9], in airborne applications [10] such as indoor localization in sensor networks [11], [12] and 3D gesture recognition systems [13], and, massively, in ultrasonic medical imaging [14]. Compared to RF waves in the industrial, scientific and medical (ISM) and medical implant communications service (MICS) bands, commonly used for connecting medical implants, ultrasonic

A preliminary, shorter version of this paper [1] appeared in the Proceedings of IEEE INFOCOM 2014.

G. E. Santagati and T. Melodia are with the Department of Electrical and Computer Engineering, Northeastern University, Boston, MA. e-mail: {santagati,melodia}@ece.neu.edu.

This material is based upon work supported by the National Science Foundation under grant CAREER CNS-1253309.

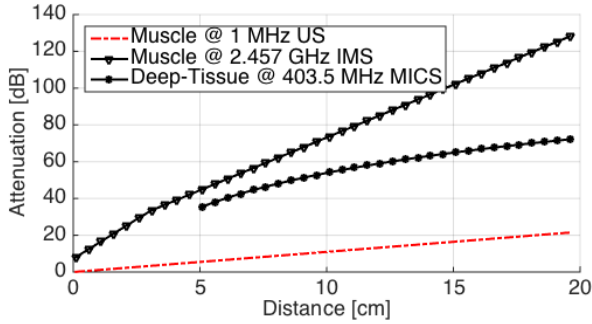


Fig. 1. Ultrasonic attenuation in human muscle for 1 MHz compared with RF attenuation for 2.45 GHz ISM Band and 403.5 MHz MICS Band.

waves have significantly lower absorption in human tissues. For example, as shown in Fig. 1, attenuation for ultrasonic waves at 1 MHz is around 10–20 dB over a 10–20 cm link in human muscle tissue, as compared to 75–130 dB attenuation for 2.45 GHz RF waves in the ISM band and 55–75 dB attenuation for 403.4 MHz RF waves in the MICS band [15], [16], [6].

Innovations in piezoelectric materials and fabrication methods have made miniaturized transducers, at the micro [17] and even nano scales [18] a reality. Moreover, the medical experience of the last decades has demonstrated that ultrasonic heat dissipation in tissues is minimal compared to RF [19], and that ultrasounds are fundamentally safe, as long as acoustic power dissipation in tissue is limited to specific safety levels [20], [6], [7]. For this reason, the FDA also allows much higher intensity for ultrasonic waves (720 mW/cm^2) in tissues as compared to RF (10 mW/cm^2) [21].

In [6], [7], we showed that intra-body ultrasonic propagation is severely affected by multipath caused by the inhomogeneity of the body in terms of density, sound speed, and the pervasive presence of small organs and particles. Based on these observations, in [8], we proposed Ultrasonic Wide-Band (UsWB), a new ultrasonic multipath-resilient physical and medium access control (MAC) layer integrated protocol. UsWB is based on the idea of transmitting short carrierless ultrasonic pulses following a pseudo-random adaptive time-hopping pattern, with a superimposed adaptive spreading code. Impulsive transmission and spread-spectrum encoding combat the effects of multipath and scattering and introduce waveform diversity among interfering nodes so that multiple users can coexist with limited interference on the same channel.

Compared to RF-based wireless technologies such as Bluetooth or Wi-Fi, UsWB has significantly lower absorption by human tissues; therefore, lower transmission power is needed, and implantable battery-powered devices may last longer and/or be smaller in size. With UsWB, patients will benefit from implants that provide wireless telemetry and reprogrammability while minimally affecting the battery lifetime of the device. This reduces the number of surgical procedures required to replace the implant. UsWB can also provide telemetry with frequent readings, i.e., continuous real-time monitoring and transmission of physiological parameters, which is not possible with RF-based current technologies

without rapidly depleting the battery. In this way, UsWB will enable monitoring applications that will reduce in-office visits and hospitalization, leading to substantial savings in medical costs. From a security and reliability perspective, the UsWB protocol cannot be easily eavesdropped or jammed without physical contact. Additionally, it eliminates electromagnetic compatibility concerns of a crowded RF spectrum. It is therefore safer and transparent to the RF spectrum management procedures of healthcare facilities.

As of today, *there have been no attempts at experimentally demonstrating ultrasonic communications through body tissues*. In this paper, we make the following core contributions: (i) we present the *design and implementation of a software-defined testbed* architecture for ultrasonic intra-body area networks. The testbed consists of software-defined nodes communicating via ultrasonic waves through media that emulate acoustic propagation through biological tissues with high fidelity, i.e., ultrasonic phantoms; (ii) we *experimentally demonstrate the feasibility of ultrasonic communications in human tissue mimicking material*. To this purpose, we design an FPGA-based prototype implementation of the UsWB physical and medium access control protocols and evaluate extensively its performance through a human-kidney phantom. We show that our prototype can flexibly trade data rate performance for power consumption, and achieve, for bit error rates (BER) no higher than 10^{-6} , either (i) high-data rate transmissions up to 700 kbit/s at a transmit power of -14 dBm ($\approx 40 \mu\text{W}$), or (ii) low-data rate and lower-power transmissions down to -21 dBm ($\approx 8 \mu\text{W}$) at 70 kbit/s (in addition to numerous intermediate configurations). Moreover, we show how the UsWB MAC protocol allows multiple concurrent users to coexist and dynamically adapt their transmission rate to channel and interference conditions to maximize throughput while satisfying predefined reliability constraints, e.g., maximum packet drop rate; (iii) we show how UsWB can enable *video monitoring medical applications for implantable devices*, and we evaluate the application video streaming performance in terms of peak signal-to-noise ratio (PNSR) and similarity (SSIM) index; finally, (iv) *we propose and validate through measurements a statistical model of small-scale fading for the ultrasonic intra-body channel*. Specifically, we show that the amplitude distribution of the signal received through human-kidney phantoms follows a generalized Nakagami distribution;

The remainder of the paper is organized as follows. In Section II we present the related work. In Section III we briefly discuss basic aspects of ultrasonic intra-body communications and introduce the UsWB transmission and medium access technique. In Section IV we present the proposed testbed architecture. In Section V we discuss the communication system architecture and implementation while in Section VI we discuss details of the FPGA implementation of transmitter and receiver. In Sections VII we extensively evaluate the performance of UsWB. In Sections VIII and IX we discuss a video monitoring application based on UsWB and a statistical model of small-scale fading for the ultrasonic intra-body channel. Finally, in Section X we conclude the paper.

II. RELATED WORK

IEEE 802.15.6 [22] is the first international standard for Wireless Body Area Network (WBAN) to enable communication and networking inside the human body. The standard defines a MAC layer based on slotted ALOHA or Carrier Sensor Multiple Access/Collision Avoidance (CSMA/CA) protocol, and three PHY layers, i.e., a Narrowband (NB) PHY, an UltraWide Band (UWB) PHY and a Human Body Communication (HBC) PHY that uses the human body itself as transmission medium for electrical signals. The use of UWB communications for medical application has been previously proposed [23], also for specific monitoring applications such as wireless capsule endoscopy [24]. Alternatively, HBC have been investigated for intra-body communications using both capacitive coupling [25] and galvanic coupling [26] where the information is modulated either by an electrical potential or a current flow.

The idea of using ultrasonic waves for intra-body communications has been proposed also in [27], [20], [28]. In [27] the authors present a propagation model for ultrasonic communication in human tissues, while in [20] the authors present a feasibility study of ultrasonic communications in nanoscale between implantable nanorobots. However, no specific communication schemes and protocols have been proposed, and no experimental evaluation has been carried to prove the feasibility of ultrasonic intra-body communications. In [28], the authors investigate the use of ultrasonic waves to communicate with an implanted device from an external unit using backscattering modulation only.

In [8], we proposed Ultrasonic WideBand (UsWB), a new ultrasonic multipath-resilient physical and medium access control (MAC) layer integrated protocol. UsWB is based on the idea of transmitting short carrierless ultrasonic pulses following a pseudo-random adaptive time-hopping pattern, with a superimposed adaptive spreading code. In this paper, we experimentally demonstrate the feasibility of ultrasonic communications in human tissue mimicking material, and we show that the UsWB physical and medium access control protocols enable nodes to flexibly trade data rate performance for power consumption, and allow multiple concurrent users to coexist by dynamically adapting their transmission rate to channel and interference conditions.

III. BACKGROUND

A. Ultrasonic Intra-Body Communications

Ultrasounds are mechanical waves that propagate in an elastic medium at frequencies above the upper limit for human hearing, i.e., 20 kHz.

Attenuation. Two main mechanisms contribute to ultrasound attenuation in tissues, i.e., absorption and scattering. An initial pressure P_0 decays at a distance d according to [29]

$$P(d) = P_0 e^{-\alpha d}, \quad (1)$$

where α (in $[\text{Np} \cdot \text{cm}^{-1}]$) is an amplitude attenuation coefficient that captures all the effects that cause dissipation of energy from the ultrasound wave. Parameter α depends on the carrier frequency through $\alpha = a f^b$, where f represents the

carrier frequency (in MHz) and a (in $[\text{Np} \cdot \text{m}^{-1} \cdot \text{MHz}^{-b}]$) and b are attenuation parameters characterizing the tissue [6], [7].

Propagation Speed. Ultrasonic wave propagation is affected by propagation delays that are orders of magnitude higher than RF. The propagation speed of acoustic waves in biological tissues is approximately 1500 m/s, as compared to 2×10^8 m/s [30] for RF waves.

Operating Frequency. Key considerations in determining the operating frequency are (i) the frequency dependence of the attenuation coefficient, and (ii) the frequency dependence of the beam spread of ultrasonic transducers (which is inversely proportional to the ratio of the diameter of the radiating surface and the wavelength [6], [7]). Therefore, higher frequencies help keep the transducer size small, but result in higher signal attenuation. Since most biomedical sensing applications require directional transducers, one needs to operate at the lowest possible frequencies compatible with small-size transducers and required signal bandwidth. In [6], [7], we showed that for propagation distances in the order of several cm the operating frequency should not exceed 10 MHz.

Reflections and Scattering. The human body is composed of different organs and tissues with different sizes, densities and sound speeds. Therefore, it can be modeled as an environment with pervasive presence of *reflectors* and *scatterers*. The direction and magnitude of the reflected wave depend on the orientation of the boundary surface and on the acoustic impedance of the tissues [6], [7], while scattered reflections occur when an acoustic wave encounters an object that is relatively small with respect to its wavelength or a tissue with an irregular surface. Consequently, the received signal is obtained as the sum of numerous attenuated, possibly distorted, and delayed versions of the transmitted signal.

B. Ultrasonic WideBand

Based on these observations, in [8] we proposed Ultrasonic WideBand (UsWB), a new impulse-radio inspired ultrasonic transmission and multiple access technique based on the idea of transmitting short information-bearing carrierless ultrasonic pulses, following a pseudo-random adaptive time-hopping pattern with a superimposed spreading code of adaptive length. Impulsive transmission combats the effects of multipath and scattering, e.g., intersymbol interference (ISI). In fact, when replicas of pulses reflected or scattered are received with a differential delay at least equal to the pulse width, they do not overlap in time with the original pulse. Therefore, for pulse durations in the order of hundreds of nanoseconds, pulse overlaps in time (ISI) are reduced and multiple propagation paths can be efficiently resolved and combined at the receiver to reduce the bit error rate. Moreover, the low duty cycle of pulsed transmissions reduces the impact of thermal and mechanical effects of ultrasounds in tissues, which could potentially be detrimental for human health.

Physical Layer. Consider, as in Fig. 2, a slotted timeline divided in slots of duration T_c , with slots organized in frames of duration $T_f = N_h T_c$, where N_h is the number of slots per frame. Each user transmits one pulse per frame in a slot determined by a pseudo-random *time-hopping sequence*. Information is carried through pulse position modulation (PPM),

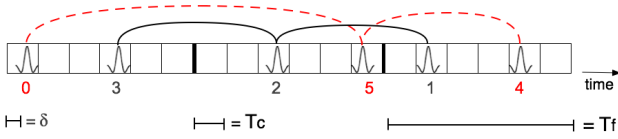


Fig. 2. Two concurrent transmissions with $N_h = 6$, $N_s = 3$, time-hopping sequences $\{3, 2, 1\}$ and $\{0, 5, 4\}$ and spreading codes $\{1, 1, -1\}$ and $\{1, -1, -1\}$.

i.e., a ‘1’ symbol is carried by a pulse delayed by a time δ with respect to the beginning of the slot, while a ‘-1’ symbol begins with the slot. Since a single pulse may collide with pulses transmitted by other users with a probability that depends on the frame size N_h , we represent each information bit with *pseudo-orthogonal spreading codes of variable length*, N_s because of (i) their excellent, and well-understood multiple access performance, (ii) limited computational complexity, and (iii) inherent resilience to multipath. The resulting transmitted signal for a symbol d can be modeled as

$$s(t) = \sum_{j=0}^{N_s-1} p\left(t - c_j T_c - j T_f - \frac{a_j d + 1}{2} \delta\right) \quad (2)$$

where $p(t)$ is the pulse shape, $\{c_j\}$ is the time-hopping sequence with $0 \leq c_j \leq N_h - 1$, $\{a_j\}$ is the pseudo-orthogonal spreading code of N_s chips with $a_j \in \{-1, 1\}$, and δ is the PPM shift of a pulse representing a ‘1’ chip.

Medium Access Control. The low-duty-cycle impulse-based transmission scheme with a superimposed spreading code allows multiple transmitters to coexist on the same channel. In UsWB, by dynamically and distributively adapting their time-hopping frame length and spreading code length, multiple users coexist without the need for mutual temporal exclusion between different transmissions (which is hard to achieve in ultrasonic channels affected by long propagation delays). By adapting frame and code length, users control the tradeoffs among (i) resilience to multi-user interference and ultrasonic channel errors, (ii) achievable information rate, and (iii) energy efficiency. As discussed in detail in [8], by controlling the time-hopping frame length N_h , i.e., the average inter-pulse time, a user can adapt the transmission rate (which decreases with larger time-hopping frame), and as a consequence modify the average radiated power and therefore the level of interference generated to other ongoing communications. By controlling N_s , i.e., the number of pulses per information bit, a user can control the tradeoff between robustness to multi-user interference and noise (which increases with longer spreading codes), energy consumption per bit (which increases linearly with increasing N_s) and information rate (decreasing with increasing N_s). UsWB optimally, distributively, and asynchronously regulates these tradeoffs to (i) maximize the communication rate, or (ii) minimize the energy consumption.

In this paper, we consider the rate-maximizing adaptation in [8], where each user distributively maximizes its transmission rate by selecting an optimal pair of code and frame lengths based on the current level of interference and channel quality for a given maximum tolerable BER. Rate adaptation is achieved through an ad-hoc designed protocol. A two-way handshake opens the connection between two nodes, T_x and

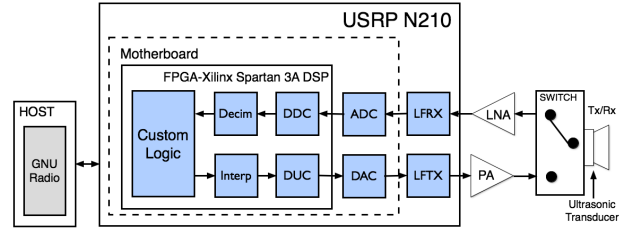


Fig. 3. Hardware architecture of an ultrasonic software-defined node.

R_x . T_x sends a Request-to-Transmit (R2T) packet to R_x . If R_x is idle, a Clear-to-Transmit (C2T) packet is sent back to T_x . Once the connection has been established, the receiver R_x estimates the interference and calculates the frame and spreading code lengths that maximize the communication throughput, as discussed in detail in [8]. This information is piggybacked into ACK or NACK packets.

IV. ULTRASONIC TESTBED ARCHITECTURE

We designed and implemented a reconfigurable platform to test ultrasonic communication and networking schemes. The testbed consists of ultrasonic software-defined nodes communicating through ultrasonic phantoms that emulate acoustic propagation through biological tissues with high fidelity. The proposed hardware architecture of an ultrasonic software-defined node is illustrated in Fig. 3. It consists of (i) a Universal Software Radio Peripheral (USRP) N210, (ii) a host machine, (iii) an electronic switch, (iv) an amplification stage, (v) and a high-frequency ultrasonic transducer.

USRP N210. Several Software Defined Radio (SDR) development platforms are available [31], [32] where Field-Programmable Gate Arrays (FPGAs) or specialized processors are used for high-sample-rate digital signal processing. Among these, we selected USRP [31] because of its low cost and wide adoption in academia and industry. USRP N210 consists of a motherboard and two daughterboards. The motherboard is the main processing unit, and incorporates AD/DA converters (a dual 100 MSPS 14-bit ADC and a dual 400 MSPS 16-bit DAC), and an FPGA unit (Spartan 3A-DSP 3400). The daughterboards are RF front-ends that interface the device with transmitter or receiver antennas. We use LFTX and LFRX daughterboards, that operate from DC to 30 MHz, which includes ultrasonic frequency ranges of interest to us.

In USRP, the system complexity is shifted from hardware to software and most of the computational load is typically left to the host machine. However, recent literature [33], [34] has shown that the host machine can become the computational bottleneck of the communication system, while the connection between host and USRP introduces delays preventing accurate timing of network protocols. As discussed in detail in what follows, we overcome this problem by shifting (with respect to the typical GNU Radio/USRP architecture) significant components of the signal processing on the on-board FPGA.

Host Machine. The host machine can be either a desktop/laptop computer or a computer-on-module, e.g., Gumstix, connected to the USRP through a Gigabit Ethernet (GbE) link. In the traditional GNU Radio/USRP architecture, the host machine runs all the software-defined signal processing

functionalities implemented with the GNU Radio development toolkit [35]. However, for reasons discussed in detail in Section V, we chose to implement most PHY and MAC functionalities in the FPGA embedded in the USRP. Therefore, in our design the host machine only configures and initializes the USRP, and generates/receives application-layer bit streams.

Electronic Switch. To reduce the testbed complexity and cost, we use an electronic switch that allows a single ultrasonic transducer to transmit and receive on a time division basis. The switching operation is piloted both from the host machine and the USRP FPGA by connecting the switch with the General Purpose Input/Output (GPIO) digital pins available on the LFTX and LFRX daughterboards. We use a commercial off-the-shelf (COTS) switch, Mini-Circuits ZX80-DR230+ [36], that comes in a connectorized package with embedded coaxial RF connectors, and offers low insertion loss and very high isolation over the entire frequency range (0 – 3 GHz).

Amplification Stage. We introduced an external amplification stage. The low-power output of the LFTX daughterboards, about 3 dBm (≈ 2 mW), can limit the maximum transmission range supported. Therefore, at the transmitter we use a connectorized COTS Power Amplifier (PA), Mini-Circuits ZPUL-30P [36], specifically designed for short-pulse transmissions with a maximum output power of 22 dBm. In the receiver chain, LFRX daughterboards have no gain (0 dB). Thus, we use a connectorized COTS Low-Noise Amplifier (LNA), Mini-Circuits ZFL-1000LN+ [36], with a noise figure of 2.9 dB.

Ultrasonic Transducers. An ultrasonic transducer is a device capable of transmitting and receiving ultrasonic waves. Most commercial ultrasonic transducers are based on the piezoelectric effect, which allows converting electrical energy in ultrasonic energy, and vice versa [37].

As discussed in Section III-A, to communicate in human tissues over a range of several centimeters we need transducers operating at frequencies in the order of a few MHz. Moreover, high-bandwidth transducers are necessary to implement wideband transmission schemes such as UsWB. We found that the only COTS ultrasonic transducers that nearly match our requirements are those designed for nondestructive analysis (NDA) applications [38], since high frequencies and large bandwidth are required for fine material characterization. However, these transducers are not optimized in terms of coupling electromechanical efficiency, and thus introduce significant energy conversion losses. Moreover, NDA transducers are characterized by high directivity. Directional transducers allow to reduce the multipath effect caused by the channel reflections and scattering, and to maximize the energy efficiency of the transmission. As a drawback, directional transducers require a-priori information about the relative position between the transmitter and the receiver to successfully direct the beam. This limitation can be overcome by using array of ultrasonic transducers with beam-steering functionalities.

In our current testbed we use *standard immersion W-series ultrasonic transducers*, *Ultran WS37-5* [38]. The piezoelectric element responsible of the energy conversion is composed of Lead Zirconate Titane (PZT) and Lead Magnesium Niobate (PMN), and it has a diameter of 9.5 mm. The nominal bandwidth central frequency is about 5 MHz and the bandwidth



Fig. 4. Human-kidney phantom immersed in a background water-based gel.

at -6 dB goes from 50% to 100% of the bandwidth central frequency, i.e., 2.5–5 MHz. Furthermore, the standard immersion W-series is designed to operate in contact with water, thus they represent the best available solution for communication in water-based media, such as the biological tissues.

Ultrasonic Phantoms. We use ultrasonic phantoms to emulate the intra-body ultrasonic communication channel with high fidelity [39]. Commonly employed in medical ultrasound research, ultrasonic phantoms are composed of soft and hard tissue-mimicking materials, also known as tissue substitutes. These materials have the same acoustic propagation properties of human tissues, e.g., sound speed, density, and attenuation. Off-the-shelf ultrasonic phantoms that emulate the interactions between ultrasounds and the human body, tissues, organs and systems are available [40].

We selected a human-kidney phantom immersed in a background water-based gel [40], as shown in Fig. 4, whose acoustic characteristics are reported in Table I. The background gel is almost lossless, and has the same density and sound speed as the kidney. Therefore, reflections and refractions are minimum between the kidney and the gel. Thus, the latter can be considered acoustically transparent. The phantom dimensions are approximately $10 \times 16 \times 20$ cm.

TABLE I
ULTRASONIC PHANTOM ACOUSTIC CHARACTERISTICS

Tissue	Speed, v	Attenuation, α	Density, ρ
Background Gel	1550 m/s	< 0.1 dB/cm	1020 Kg/m ³
Kidney	1550 m/s	2 dB/cm @ 5 MHz	1030 Kg/m ³

V. ARCHITECTURE OF THE COMMUNICATION SYSTEM

Signal processing, algorithms and protocols can be implemented in the ultrasonic software-defined node using a framework that combines (i) the GNU Radio software development toolkit [35] and (ii) the open source Hardware Description Language (HDL) design for the FPGA embedded in the USRP. In GNU Radio, most of the digital signal processing is performed on the external host. When using HDL design most signal processing operations are moved to the embedded FPGA. In this Section we discuss the tradeoffs between these two different approaches.

A. GNU Radio Vs. HDL PHY Layer Implementation

As discussed in Section III-B, wideband pulse-based communications can significantly mitigate the multipath effect

caused by the heterogeneity of the human body. However, shorter pulses have wider bandwidth, which results in higher sampling rates that can overload the host machine or the Gigabit Ethernet (GbE) link between the host machine and the USRP. In our initial design, UsWB PHY layer functionalities were implemented on the host machine using GNU Radio. However, we observed the following limitations: (i) the capacity of the GbE link between the host machine and the USRP limits the maximum achievable sample rate, i.e., 25 million samples per second, thus the maximum achievable signal bandwidth. When exceeding the link capacity, Ethernet frames coming from/to the USRP are dropped at the network interfaces, with consequent loss of the carried digital samples; (ii) digital signal processing operations implemented in GNU Radio, e.g., digital filters, overload the host machine when operating at high sampling rates, i.e., greater than 10 million samples per second. If the host machine is unable to process data fast enough, the internal buffers that store digital samples overflow, thus causing loss of large amount of digital samples.

It became apparent that the above limitations would prevent successful implementation of UsWB in GNU Radio. For these reasons, we chose to implement all PHY layer functionalities in the embedded FPGA. This effectively speeds up data processing and reduces the computational load on the host machine.

Partial Reconfiguration. The price we pay for these benefits is a lower system flexibility. The HDL design needs to be synthesized before it can be loaded in the embedded FPGA. Thus, changing the PHY layer structure and parameters at runtime is not as simple as doing it in GNU Radio on the host machine. Still, we designed the HDL modules such that partial PHY layer reconfiguration is achievable at runtime through a group of setting registers implemented on the FPGA that can be accessed by the host machine. Through these setting registers, one can reconfigure key parameters of the PHY layer transmission scheme (i.e., pulse shape and code length, among others) or even select which PHY blocks should be used, thus modifying at runtime the structure of the PHY layer chain.

B. MAC Layer Design Challenges

Similarly, MAC-layer functionalities can potentially be implemented in the host machine or in the embedded FPGA. Highly customized or reconfigurable and complex protocols can be challenging to implement on FPGA and likely cause overutilization of the available FPGA hardware resources. An appealing alternative is then to implement the MAC layer on the host machine, by using high-level languages and libraries available in GNU Radio. However, MAC protocols require highly precise packet timing and small, precise inter-frame spacings in the order of microseconds. We observed that GbE link and the GNU Radio processing latency are in the order of milliseconds [34]. Hence, time-critical radio or MAC functions cannot be placed in the host machine. Hybrid solutions, based on soft-core processors implemented in the embedded FPGA (e.g., Microblaze, ZPU) running software-defined protocols [34], [41] are also possible. Protocols and algorithms can be implemented using high level programming languages, e.g., C or C++, and then executed inside the FPGA.

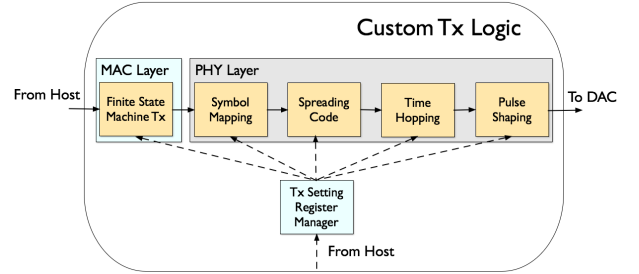


Fig. 5. Block scheme of the custom transmitter logic.

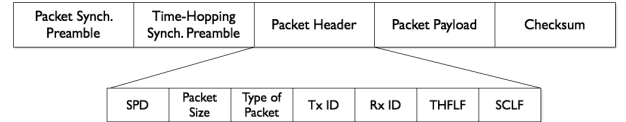


Fig. 6. UsWB MAC layer packet structure.

In the current system architecture the MAC layer is implemented in HDL, and the FPGA setting registers enable partial reconfiguration at runtime. We are currently working on the implementation of a hybrid solution [34], [41] based on a soft-core processor implemented in the embedded FPGA.

VI. TX AND RX HDL ARCHITECTURE

The default USRP HDL design operates on digital waveforms coming from and going to the host machine and performs only digital down and up conversion (DDC/DUC), decimation and interpolation. PHY and MAC layer digital processing takes place on the host machine. We followed a different approach, and we customized and extended the USRP HDL code to implement UsWB PHY and MAC layer operations in the FPGA.

A. Custom Transmitter Chain

Figure 5 shows a block diagram of the custom transmitter logic. Since PHY and MAC functionalities are implemented on the FPGA, input data are raw information bits that need to be packetized and encoded in digital waveforms. After MAC and PHY layer operations, the custom transmitter logic outputs the digital quantized signal to be transmitted. This is then digital-to-analog converted, amplified and finally converted into an ultrasonic signal by the transmitter transducer.

Transmitter MAC Finite State Machine. The UsWB MAC-layer data structure, i.e., UsWB packet¹ is created in the FSM-TX. The UsWB packet is then serialized, i.e., converted into a sequence of bits, and forwarded to the next module in the chain, i.e., Symbol Mapping. The FSM-TX also controls the time-hopping frame length N_h and spreading code length N_s used by the PHY layer, according to feedback information from the receiver.

In Fig. 6 we show the UsWB packet structure. The UsWB packet starts after a Packet Synchronization Preamble (PSP) and a Time-Hopping Synchronization Preamble (THSP). The

¹We intentionally use the word *packet* instead of *frame* to avoid confusion with the time hopping frame in Section III-B.

former enables coarse synchronization that allows the receiver to detect an incoming packet, while the latter allows identifying the exact start time of the time-hopping frame. The packet header is delimited by a 16-bit Start Packet Delimiter (SPD). This is followed by a 16-bit MAC Packet Size field representing the payload length in bytes. Then, a 3-bit Type of Packet is used to distinguish between R2T and C2T packets, ACK and NACK packets, and data packets. This is followed by two 6-bit fields representing the transmitter and receiver ID. Finally, an 8-bit Time-Hopping Frame Length Feedback (THFLF) and an 8-bit Spreading Code Length Feedback (SCLF) contain the feedback values piggybacked in ACK or NACK packets. A 16-bit packet checksum follows the payload to verify that the packet has been received correctly.

The UsWB packet is then serialized, i.e., converted into a sequence of bits, and forwarded to the next module in the chain, i.e., Symbol Mapping. The FSM-TX also controls the time-hopping frame length N_h and spreading code length N_s used by the PHY layer, according to feedback information from the receiver.

Transmitter PHY Layer. The first block of the transmitter PHY layer chain is Symbol Mapping. Here, raw information bits are mapped into $\{-1,1\}$ binary symbols. The binary symbols are then spread in chips by the Spreading Code module following a pseudo-random spreading code. For each symbol, this block outputs N_s chips in $\{-1,1\}$. Chips are then forwarded to the Time-Hopping module that spreads them in time according to the selected time-hopping pattern. The output of this block is a sequence of $\{-1,1\}$ chips, one per time-hopping frame. Finally, the Pulse Shaping module maps the incoming chips to position-modulated pulses. The output is a train of position-modulated pulses following a predefined time-hopping pattern, as described in (2).

Pulse Shaping. The Pulse Shaping module consists of a Finite Impulse Response (FIR) filter whose coefficients, i.e., taps, represent the samples of a 4th-order derivative gaussian pulse. The original design discussed in [8] was based on a 2nd-order derivative gaussian pulse. However, to match the central frequency and bandwidth requirements of the ultrasonic transducers in use, we adopted a higher-order derivative gaussian pulse characterized by higher central frequency and lower relative bandwidth [42]. In Fig. 7a and Fig. 7b the two pulse shapes are compared in the time and frequency domains. Figure 7b also shows a 4th-order derivative pulse shaped to match the frequency response of the Ultran WS37-5 ultrasonic transducer. The pulse duration is approximately 300 ns, with a PPM shift of 60 ns, within a time-hopping slot (T_c in Section III-B) of 360 ns. The resulting maximum raw chip rate is 2.78 Mchip/s, which results in a maximum raw data rate of 2.78 Mbit/s when time-hopping frame and spreading code lengths are both set to 1.

Transmitter Setting Register Manager. The Transmitter Setting Register Manager (SRM-Tx) is in charge of routing configuration parameters written by the host machine into the setting registers discussed in Section V-A. Whenever the host machine updates any of the setting registers, the SRM-Tx is triggered to read the register content and route it to the destination module. This block enables real-time

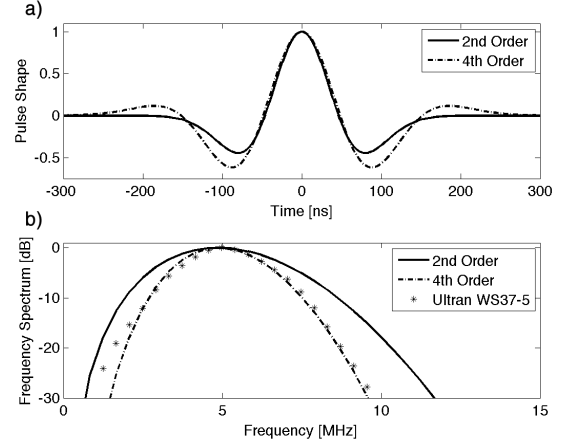


Fig. 7. a) 2nd-order and 4th-order derivative gaussian pulses, b) compared in frequency domain with the Ultran WS37-5 frequency response.

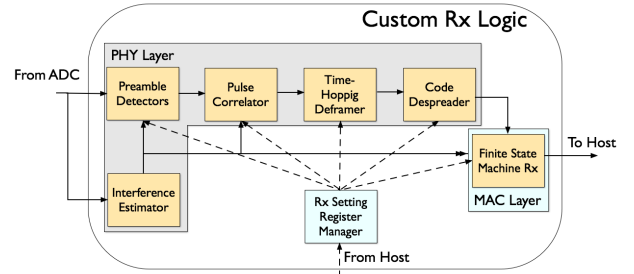


Fig. 8. Block scheme of the custom receiver logic.

reconfiguration thus enhancing the transmitter flexibility.

The communication system is designed to allow real-time reconfiguration of several parameters, i.e., spreading code and spreading code length, time-hopping frame length and time-hopping sequence, packet payload size, SPD sequence and SPD length, and length of the preambles. One can also change the pulse shape in real time through FIR filters with reloadable taps. Moreover, by carefully rerouting the binary flow, we can use the registers to enable and disable selected modules to reconfigure in real time the entire chain structure, thus modifying the communication system architecture. For example, we can implement adaptive modulation by switching between different Symbol Mapping modules at runtime to change the symbol constellation used. Moreover, we can disable the Time-Hopping module or the Spreading Code module to obtain pure spreading-code or time-hopping based schemes.

B. Custom Receiver Chain

The custom receiver chain, illustrated in Fig. 8, implements receiver UsWB PHY and MAC layer functionalities. The received ultrasonic signal is converted to an electrical signal by the RX transducer. The signal is amplified by the LNA, and analog-to-digital converted by the USRP ADC. Then, the digital waveform is processed by the custom receiver chain in the FPGA. After PHY and MAC operations, the custom receiver chain outputs a binary stream representing the received decoded data.

Receiver MAC Finite State Machine. The Receiver MAC Finite State Machine (FSM-RX) implements UsWB MAC protocol functionalities and coordinates the PHY-layer logic.

The FSM-RX detects the received packet based on information coming from preamble detectors, and triggers the PHY layer module to start processing the received waveform. Finally, it decodes the received bits based on the output of the PHY layer operations on the received digital waveforms. Moreover, FSM-RX estimates the level of interference, and accordingly chooses the optimal pair of time-hopping frame length and spreading code length, i.e., those that maximize the communication throughput while keeping the bit error rate (BER) under a predefined threshold - see [8] for details.

Preamble Detectors. The preamble detectors are designed to achieve *packet* and *time-hopping* synchronization. The former enables coarse synchronization by identifying the presence of an incoming packet. The latter identifies the exact start point of the time-hopping frame.

The Packet Synchronization Preamble (PSP) consists of a train of pulses positioned in consecutive time slots. The PSP detector includes a single-rate FIR filter used as a correlator, a squaring module, an integrator, and a threshold-based plateau detector. The FIR filter is used to correlate the incoming pulses with a 5th-order derivative gaussian pulse, the filter impulse response. Squaring and integrating the correlator output ideally results in a constant output for the whole PSP duration, i.e., a plateau. Therefore, the packet can be coarsely detected by finding the plateau. By using a dynamic threshold adaptation, this procedure can be made independent of the noise floor.

Fine synchronization is performed by the Time-Hopping Synchronization Preamble (THSP) detector, which includes a single-rate FIR filter used as correlator, and a threshold-based correlation peak detector. The THSP consists of a train of pulses, each positioned in the first time slot of consecutive time-hopping frames. By correlating the THSP with a 5th-order derivative gaussian pulse, we obtain a peak in the first slot of each time-hopping frame. The beginning of the time-hopping frame is determined by the threshold-based peak detector. Again, the threshold is dynamically adapted to the noise floor level.

Receiver PHY Layer. The receiver PHY layer module implements the bit decoding operations that can be formally expressed as

$$\sum_{j=0}^{N_s-1} a_j \int_{c_j T_c - j T_f}^{(c_j+1)T_c - j T_f} s(t) \cdot c(t) dt \underset{d_1}{\overset{d_{-1}}{\gtrless}} 0, \quad (3)$$

where $c(t)$ is the correlator function, while all the other symbols follow the signal model presented in Section III-B.

The first module in the receiver PHY chain is the Pulse Correlator, i.e., a decimator FIR filter with a 5th-order derivative gaussian pulse impulse response. The Pulse Correlator outputs one sample per time slot, and the FIR impulse response, i.e., the correlator function $c(t)$, is selected in such a way as to give a zero output for an empty slot, a positive value for a slot containing a ‘-1’ chip, and a negative value for a slot containing a ‘1’ chip. The correlation output goes into the Time-Hopping Deframer, which collects the non-zero inputs located according to the Time-hopping sequence used at the transmitter. The Time-Hopping Deframer determines the integral intervals and the Pulse Correlator performs the actual

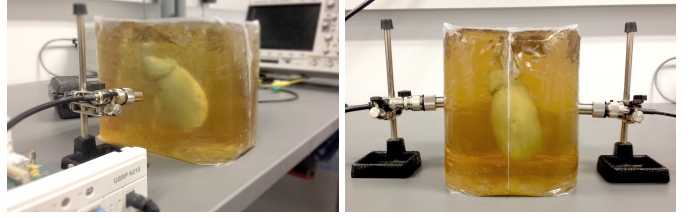


Fig. 9. Two nodes communicating through a human-kidney phantom.

integration in (3).

Finally, the Code Despreader inverts the spreading operation by weighting the correlation output with the spreading code originally used at the transmitter and summing these over the spreading code length. This operation corresponds to the weighted sum in (3). Based on the result of the despreading operation, the FSM-RX makes a decision on the received bits. If the resulting sum is positive a ‘-1’ symbol is received (d_{-1}), otherwise a ‘1’ symbol is received (d_1).

Receiver Setting Register Manager. The Receiver Setting Register Manager (SRM-Rx) provides the same functionalities as the SRM-Tx. The SRM-Rx operates on registers different than those used in the transmission chain. Therefore, the transmitter and receiver chains of each node can be independently reconfigured in real time.

Interference Level Estimation. The Interference Level Estimation module is needed by the UsWB MAC protocol to perform the rate-maximizing adaptation described in detail in [8]. The level of interference is estimated in terms of number of interfering pulses per time-hopping frame. The estimation module consists of a single-rate FIR filter whose impulse response is a 5th-order derivative gaussian pulse, a squaring module, an integrator and a peak detector with dynamically adapted threshold. By comparing at each time slot the integrator output with the threshold, we can detect the presence of pulses, and therefore how many pulses are received in a time-hopping frame. The level of interference is obtained by averaging over the entire packet reception time.

VII. USWB PERFORMANCE EVALUATION

In this section we demonstrate the feasibility of ultrasonic intra-body communications through testbed experiments. We start by evaluating the physical layer performance of the prototype we developed in terms of BER by varying the transmit power, the time-hopping frame and spreading code length and the level of interference in the channel. Then, we show how MAC adaptation allows a pair of nodes to adapt the communication rate according to the level of ultrasonic interference, to maximize the throughput while satisfying packet drop rate reliability constraints.

A. UsWB PHY Layer

The testbed setup consists of two ultrasonic software-defined nodes communicating through a human-kidney phantom (Fig. 9). The two nodes ultrasonic transducers are positioned in the opposite sides of the phantom smaller dimension, i.e., 10 cm, and the kidney is centered in the background gel

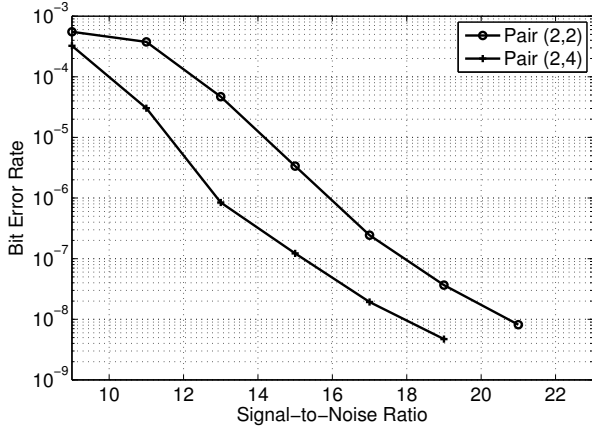


Fig. 10. BER in the absence of interference as a function of the SNR.

such to be aligned between the two ultrasonic transducers. To guarantee repeatability of the experiments, we generate interference from co-located transceivers artificially by injecting interfering pulses at the transmitter. The position of the interfering pulses inside the time-hopping frame is given by a pseudo-random generator HDL module, i.e., a Linear Feedback Shifter Register (LFSR). Moreover, the interfering pulses are not synchronized with the time slots of the communicating pair.

BER Vs SNR. First, we evaluate the BER as a function of the *SNR per pulse* measured at the receiver, in the absence of external interference, with fixed time-hopping frame and spreading code length. We define the *SNR per pulse* as the ratio between the energy per pulse E_p and the noise power spectral density η

$$SNR = \frac{E_p}{\eta} = \frac{P_R T_p}{P_N / B} \quad (4)$$

where P_R is the received signal power, T_p is the pulse duration, P_N is the receiver noise power and B is the transmission bandwidth.

By connecting a variable-gain attenuator between the LFTX daughterboard and the power amplifier we vary the input power at the Tx transducer between -7 dBm ($200 \mu\text{W}$) and -21 dBm ($8 \mu\text{W}$), to obtain values of SNR between 23 and 9 dB, respectively. Note that the transmission power levels in use lead to ultrasonic radiation in tissue that is orders of magnitude below the maximum limits imposed by the FDA [21]. In Fig. 10, the resulting BER is depicted for time-hopping frame length and spreading code length pairs (2,2) and (2,4). We observe that, as expected, the BER is a decreasing function of the SNR and that by using longer spreading code the BER is further reduced. If we further decrease the SNR at the receiver, i.e., to 7 dB (a transmit power of -23 dBm), communication fails altogether due to limitations in the current time synchronization scheme. In the considered “kidney” setup, the UsWB prototype achieves 347.21 kbit/s with a 10^{-6} BER at 13 dB SNR, which corresponds to an input power at the Tx transducer of about -17 dBm ($\approx 20 \mu\text{W}$). A data rate up to about 700 kbit/s can be achieved (also with 10^{-6} BER) with a (2,2) pair increasing the input power to -14 dBm ($\approx 40 \mu\text{W}$),

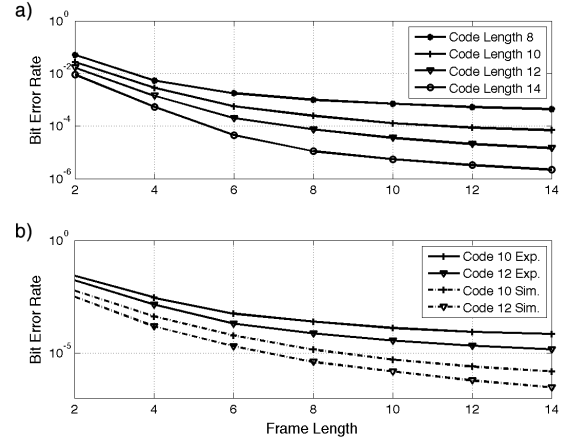


Fig. 11. BER as a function of frame length, with 4 interfering pulses per frame for different values of code length (top), compared with simulated BER (bottom).

i.e., 16 dB SNR. Lower-power transmissions are also possible by compensating with longer spreading code. For example, in the current implementation, for a Tx power of -21 dBm ($\approx 8 \mu\text{W}$), i.e., 9 dB SNR, and with a spreading code of 20 chips, we obtain a data rate of 70 kbit/s with a BER lower than 10^{-6} .

Energy conversion losses can be reduced with custom-designed ultrasonic transducers with higher coupling electromechanical efficiency to further reduce the Tx power requirements. Moreover, we acknowledge that there is significant room for improving the current time synchronization scheme, after which it will be possible to operate at even lower SNRs.

BER Vs Time-Hopping and Spreading Code. In Fig. 11 (top), we evaluate the BER by varying the time-hopping frame and spreading code length with 4 interfering pulses per frame. Since we focus on the effect of the interference, we set the the input power at the Tx transducer to 13 dBm, to create high-SNR condition, i.e., 43 dB SNR. In Fig. 11 (bottom) the experimental results are compared with BER curves obtained by simulating the same scenario with the UsWB PHY layer simulator described in [8]. For fairness, the pulse shape used in the simulator is obtained by recording a real pulse shape as received in testbed experiments. Therefore, we consider the signal distortion introduced by amplifiers and transducers, and the scattering and reflection effects introduced by the ultrasonic phantom. However, the imported deterministic measurement does not consider the time-variability of the real testbed conditions, e.g., operating temperature, humidity, and coupling of the transducer with the phantom surface, among others. We observe that, as expected, the BER is a decreasing function of the time-hopping frame length and the spreading code length, thus confirming the simulation results in our previous work [8].

BER vs Interference. We repeat the same experiment by setting the spreading code length to 4 chips, varying the time-hopping frame length and the number of interfering pulses per frame (Fig. 12). Here, we observe that the transmitter can adapt to different level of interference to satisfy the BER requirement

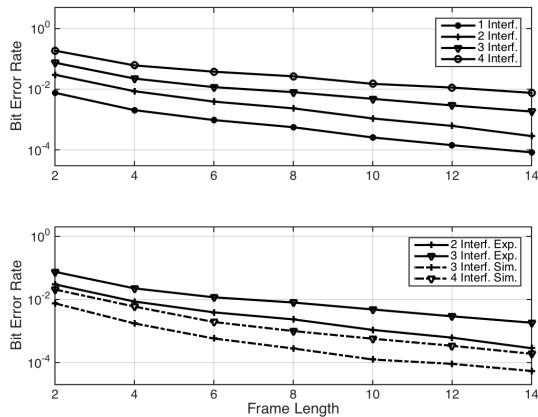


Fig. 12. a) Experimental BER as a function of time-hopping frame length, with a 4-chip spreading code for different number of interfering pulse per frame, b) compared with simulated BER.

by increasing the frame length. For example, a 10^{-3} BER for a 4-chip spreading code can be achieved with a time-hopping frame of size 8 with one interfering pulse, as well with a time-hopping frame of size 12 with two interfering pulses. The BER can be further reduced by increasing the spreading code length.

B. UsWB MAC Layer

We consider a pair of ultrasonic software-defined nodes and evaluate how the UsWB MAC protocol adapts the link parameters to compensate for varying levels of interference, i.e., multiple concurrent transmissions. The level of interference is defined in terms of number of interfering pulses within a time-hopping frame. If we assume that all nodes measure the same level of interference, that is, all network nodes are close enough to be all in the same transmission range, i.e., as in the implicitly cooperative problem in [8], the number of interfering pulses per time-hopping frame coincides with the number of co-located active Tx-Rx pairs.

UsWB Rate-Maximizing Adaptation. First, we evaluate the UsWB MAC rate-maximizing adaptation as a function of the level of interference. We transmit 250 packets and increase the level of interference every 50 packets, from zero interfering pulses per time-hopping frame to four. In Fig. 13 (bottom), we show the estimated level of interference at the receiver. We observe that the receiver occasionally overestimates the number of interferers, which however does not affect the performance in terms of packet drop rate. According to the UsWB protocol, based on the interference estimation, the receiver computes the optimal pair of time-hopping frame and spreading code length, and piggybacks these in ACK/NACK packets. In the current implementation, the optimization problem in [8] is solved offline, and the solution is then loaded into the receiver. By performing a lookup table operation, the receiver finds the optimal pair corresponding to the measured level of interference and BER requirements. Figure 13 (middle) shows the time-hopping frame and spreading code length used by the transmitter after

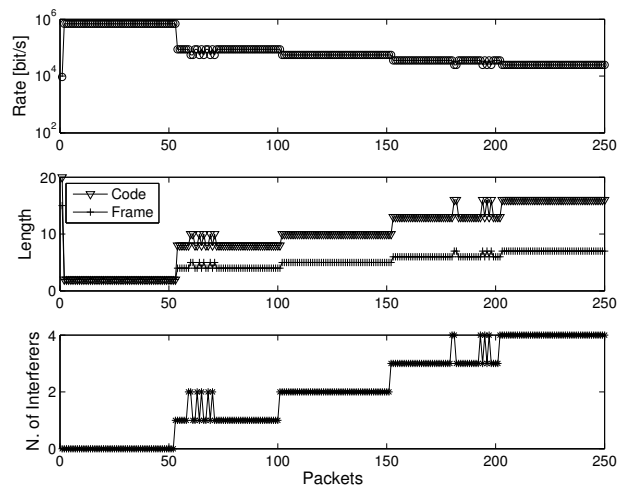


Fig. 13. Rate-maximizing adaptation. Interference estimate (top), optimal time-hopping frame and spreading code length (middle) and data rate of the transmitter (bottom).

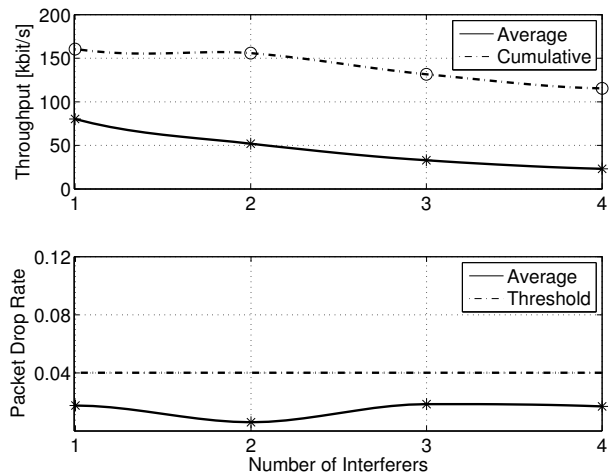


Fig. 14. Throughput (top) and packet drop rate (bottom) as a function of the number of interferers.

the ACK/NACK is received. As expected, these vary according to the interference estimate at the receiver. The resulting data rate of the transmitter is shown in Fig. 13 (top).

Throughput and Packet Drop Rate. To verify the effectiveness of the rate adaptation, we evaluate throughput and packet drop rate at the receiver while varying the level of interference. We define throughput as the average bit rate of correctly received information during a time window. The packet drop rate is defined as the ratio between the number of packets dropped and the number of packets generated at the application layer. We set the packet payload length to 512 bytes and vary the level of interference from zero to four every 5000 packets. In Fig. 14 (top), we show throughput of a single Tx-Rx pair along with the cumulative throughput considering all the concurrent interfering Tx-Rx pairs. Figure 14 (bottom) shows the resulting packet drop rate compared with the maximum packet drop rate threshold (4%) corresponding to the maximum BER constraint ($< 10^{-5}$) and packet size.

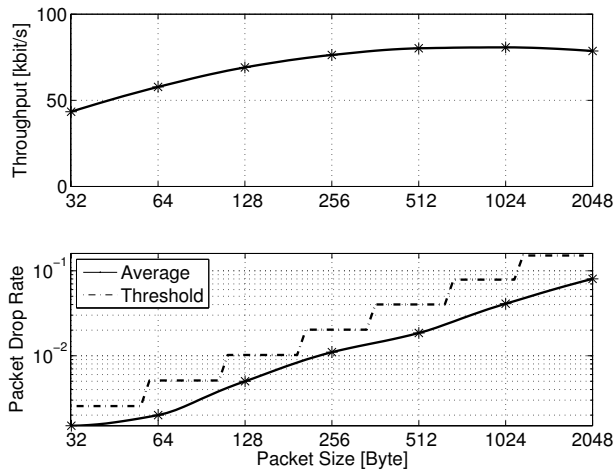


Fig. 15. Throughput (top) and packet drop rate (bottom) as a function of the packet size with one co-located interfering Tx-Rx pair.

Optimal Packet Size. Finally, we investigate how the packet size affects throughput and packet drop rate. We set the number of interferers to one, and transmit a fixed amount of data (≈ 2 MBytes) with different packet sizes. In Fig. 15 (top), we observe that the resulting throughput is maximized between 512 and 1024 bytes. The optimal packet size is influenced by the packet drop rate and protocol overhead. For a given BER, the packet drop rate is determined by the packet size, i.e., the longer the packet the higher the packet drop rate. At the same time, longer packets result in less protocol overhead (packet header, ACK/NACK control packets, and propagation delay). Figure 15 (bottom) shows that the packet drop rate increases when the payload size increases. However, the maximum packet drop rate constraint is always satisfied.

VIII. VIDEO MONITORING FOR IMPLANTABLE DEVICES

In this Section, we show how UsWB can enable video monitoring medical applications for implantable devices, and we evaluate the UsWB video streaming performance in terms of peak signal-to-noise ratio (PSNR) and similarity (SSIM) index.

Camera equipped implantable sensors can enable continuous remote monitoring of internal body organs and systems. For example, wireless capsule endoscopy (WCE) uses a pill-sized ingestible cameras to inspect the entire gastrointestinal tract and detects various anomalies, e.g, internal bleeding and tumors, among others. WCE can replace intrusive and limited examination techniques such as gastrointestinal endoscopy that are often incapable of reaching critical area of the gastrointestinal tract. Using WCE, the recorded video is wirelessly streamed in realtime from the ingestible capsule to an external image-recording belt carried by the patient. The image-recording belt receives and stores the collected video, which can be then accessed, processed and analyzed by the doctor.

We consider both the WCE and the image-recording belt to be UsWB enabled. With a data rate up to 700 kbit/s, UsWB can easily accommodate relative high quality video streaming, and the UsWB rate adaption capabilities discussed

in Section VII can be leveraged to adapt the video bitrate to the channel condition and level of interference in the channel. Moreover, an ultrasonic WEC eliminates any potential conflict with existing RF communication systems and overcrowded RF environments, and reduces the risk of potential eavesdropping and jamming attacks that can compromise the monitoring operations, and therefore the patient diagnosis.

A. Streaming Video Performance

SSIM Vs SNR Per Pulse. Here, we evaluated the video performance of an ultrasonic WCE based on UsWB in terms of PSNR and SSIM as a function of the SNR per pulse measured at the receiver, defined as in (4). The PSNR compares the maximum possible image energy to the noise energy, which has shown to have higher correlation with the subjective image quality perception than conventional SNR [43]. The SSIM index also measures the relative quality between two images, and it has been shown to be more consistent with human eye perception than PSNR [44].

In WCE, ultrasonic signals would propagate through a multilayered medium composed mainly by soft-tissues, e.g., muscle, fat and skin, among others. However, for consistency with the PHY and MAC layer results discussed in Section VII, in these experiments we use the same testbed setup shown in Fig. 9 based on a human-kidney ultrasonic phantom. Table II shows how the human-kidney captures accurately the propagation characteristics of soft-tissues media such as muscle, fat and skin [45].

TABLE II
ULTRASONIC PHANTOM ACOUSTIC CHARACTERISTICS

Tissue	Speed, v	Attenuation, α	Density, ρ
Phantom	1550 m/s	2 dB/cm @ 5 MHz	1030 Kg/m ³
Muscle	1529 m/s	0.54 dB/cm @ 4.3 MHz	1038 Kg/m ³
Fat	1487 m/s	0.56 dB/cm @ 6 MHz	939 Kg/m ³
Skin	1729 m/s	1.06 dB/cm @ 5 MHz	1110 Kg/m ³

For this experiment we selected an 11 s video from the Atlas of Gastrointestinal Video Endoscopy [46] that shows a gastroscopy of a 34 years old male's stomach. We transmit several times the video sequence over a UsWB link. At the receiver, we average the resulting PSNR and SSIM of the channel-affected received video over all the transmission repetitions. Finally, we set the UsWB packet size to be equal to 512 byte, which, as shown in Section VII-B, represents a good tradeoff between packet drop rate and protocol overhead.

In Fig. 16 we show a block scheme of the the experiment testbed setup. At the transmitter, the raw video (.yuv) is encoded in a H.264 stream using GStreamer open source multimedia framework [47], and it is temporarily stored in a FIFO memory. Our custom-made GNU Radio module reads from the FIFO memory chunks of the H.264 byte stream, and passes the resulting bitstream to the USRP devices. In the USRP, the bitstream is modulated according to the UsWB transmission scheme implemented on the embedded FPGA, converted in an ultrasonic signal through the transducers and transmitted in the ultrasonic intra-body channel, emulated through the ultrasonic phantom. At the receiver, the above

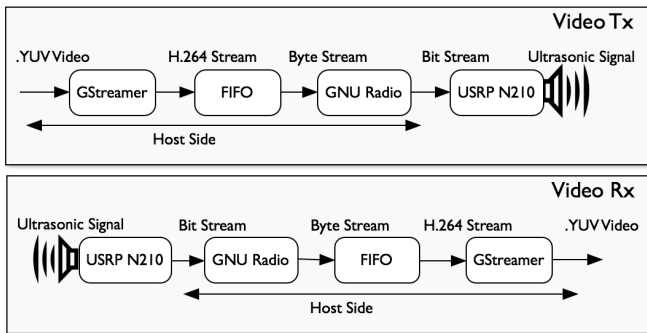


Fig. 16. Block scheme of the video streaming Tx and Rx setup.

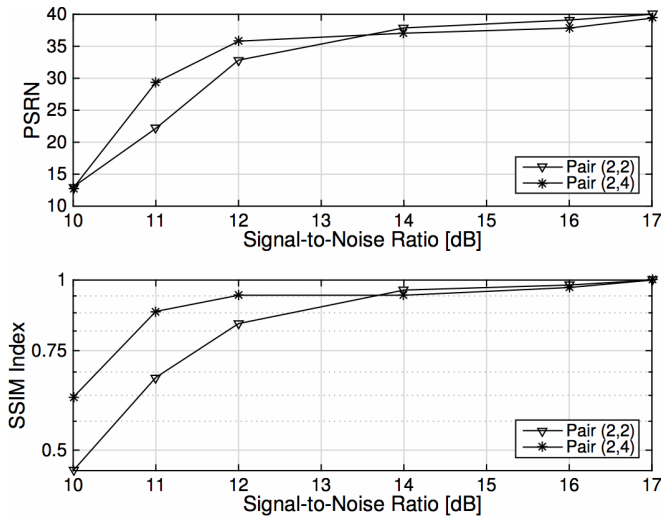


Fig. 17. PSNR (top) and SSIM (bottom) as a function of the SNR per pulse measured at the receiver for the pair (2,2) and (2,4).

operations are inverted, and the received video stream is finally analyzed in terms of PSNR and SSIM using the EvalVid video quality evaluation tool [48].

Figure 17 shows the PSNR (top) and SSIM (bottom) performances as a function of the SNR per pulse measured at the receiver, assuming frame length of 2 time slots and code length equals to 2 and 4, i.e., pairs (2,2) and (2,4). The two pairs enable data rates of approximately 700 kbit/s and 350 kbit/s, respectively. We observe that, as expected, the video quality increases with higher SNR. For SNR equal to 10dB, synchronization errors make the video quality very low (virtually no video frames are correctly visualized). For values of SNR equal to 11dB, the pair (2,4) offers relative good video quality as compared to the pair (2,2). Specifically, pair (2,4) results in PSNR equal to 30 dB, and SSIM above 0.8, which are measures of good image quality. For SNR greater or equal than 12 dB both pairs offer good image quality. Above 14 dB SNR, both pairs ensure virtually no distortion in the received images.

IX. ULTRASONIC CHANNEL CHARACTERIZATION

The ultrasonic channel can be statistically characterized through time domain measurements [49]. We use a digital sampling oscilloscope to record the response to a probing

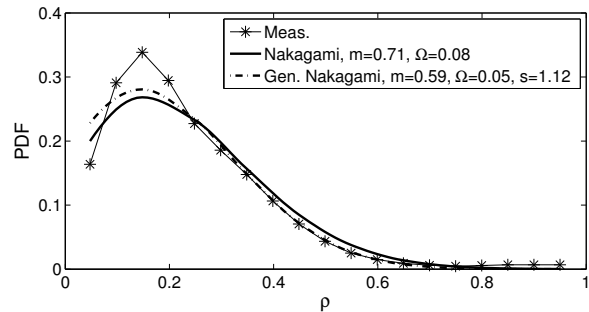


Fig. 18. Envelope amplitude distribution of the received signal fitted with a Nakagami distribution, and a generalized Nakagami distribution.

signal, and obtain a statistical model of small-scale fading for the ultrasonic intra-body channel.

Small-scale Fading Model. Small-scale fading describes variations of the channel over a period of time where the channel can be considered wide-sense stationary. In RF wireless communications, the signal envelope affected by small-scale fading has been typically modeled using different distributions, such as Rice, Rayleigh, Nakagami, Log-normal, and Weibull. We characterize the envelope of ultrasonic signals transmitted through the human-kidney phantom discussed in Section IV.

To this purpose, we transmit short ultrasonic pulses through the ultrasonic phantom, and record the output by connecting an Rx ultrasonic transducer to a digital sampling oscilloscope. We processed the collected data to identify the statistical distribution that best fits the recorded envelope distribution.

In Fig. 18 we show the recorded envelope distribution. The experimental result is least-square fitted with a Nakagami and a generalized Nakagami distribution. The probability density function (PDF) of the signal envelope ρ can then be expressed as

$$f(\rho; m, \Omega, s) = \frac{2sm^m \rho^{2sm-1}}{\Gamma(m)\Omega^m} e^{-\frac{m}{\Omega}\rho^{2s}} U(\rho) \quad (5)$$

where m is the Nakagami parameter, Ω is a scaling parameter, s is the generalization parameter, $U(\cdot)$ is the unit-step function, and $\Gamma(\cdot)$ is the gamma function. For $s = 1$, (5) gives the original Nakagami distribution.

Nakagami distribution allows to match empirical data in very general environments, under various scattering conditions. By varying the value of the Nakagami parameter m , we obtain different distributions such as Gaussian distribution ($m = 0.5$), generalized Rice distribution ($0.5 < m < 1$), Rayleigh distribution ($m = 1$) and Rice distribution ($m > 1$) [50]. Parameter s takes into account the so called *tail effect* [51]. When $s < 1$, the distribution presents heavy upper tails; for $s > 1$, we have shorter upper tails. Therefore, the Nakagami amplitude distribution can describe different scenarios by simply varying the value of m and s .

We observe that, in both cases, the values of m correspond to a generalized Rice distribution, which is typically encountered in the presence of randomly located scatterers together with periodic alignment of scatterers [50]. This is indeed the case for the human-kidney phantom used in the experiment, which consists of a scattering medium, and whose boundary

may represent potential aligned scatters. Similar results have been observed in medical ultrasonic imaging. For example, in [52] the amplitude statistics of a signal reflected from a human-kidney were modeled using a Nakagami distribution.

X. CONCLUSIONS

We discussed design and implementation of a software-defined testbed architecture for ultrasonic intra-body area networks, and experimentally demonstrated the feasibility of ultrasonic communications in tissue mimicking materials. We discussed our prototype implementation and showed that our prototype can flexibly trade performance off for power consumption, and achieve, for bit error rates (BER) no higher than 10^{-6} , either (i) high-data rate transmissions up to 700 kbit/s at a transmit power of -14 dBm ($\approx 40 \mu\text{W}$), or (ii) low-data rate and lower-power transmissions down to -21 dBm ($\approx 8 \mu\text{W}$) at 70 kbit/s. We showed how the considered MAC protocol allows multiple transmitter-receiver pairs to coexist and dynamically adapt the transmission rate according to the channel and the level of interference condition, to maximize the throughput while satisfying predefined reliability constraints. We also showed how UsWB can be used to enable a video monitoring medical application for implantable devices. Finally, we proposed (and validated through experiments) a statistical model of small-scale fading for the ultrasonic intra-body channel.

REFERENCES

- [1] G. E. Santagati and T. Melodia, "Sonar Inside Your Body: Prototyping Ultrasonic Intra-body Sensor Networks," in *Proc. of IEEE Conf. on Computer Communications (INFOCOM)*, Toronto, Canada, April 2014.
- [2] S. K. Gupta, T. Mukherjee, and K. K. Venkatasubramanian, *Body Area Networks: Safety, Security, and Sustainability*. Cambridge University Press, 2013.
- [3] St. Jude Medical, "The cardioMEMS HF system," Last access: Aug 2016. [Online]. Available: <http://www.sjm.com/cardiomems>
- [4] Medtronic, "Implantable cardioverter defibrillators (ICDs)," Last access: Aug 2016. [Online]. Available: <http://www.medtronic.com/us-en/healthcare-professionals/products/cardiac-rhythm/implantable-cardiac-defibrillators.html>
- [5] WHO/International Agency for Research on Cancer, "IARC classifies radio frequency electromagnetic fields as possibly carcinogenic to humans," May 2011, Last access: Aug 2016. [Online]. Available: http://www.iarc.fr/en/media-centre/pr/2011/pdfs/pr208_E.pdf
- [6] L. Galluccio, T. Melodia, S. Palazzo, and G. E. Santagati, "Challenges and Implications of Using Ultrasonic Communications in Intra-body Area Networks," in *Proc. of IEEE Intl. Conf. on Wireless On-demand Networked Systems (WONS)*, Courmayeur, Italy, Jan. 2012.
- [7] G. Santagati, T. Melodia, L. Galluccio, and S. Palazzo, "Ultrasonic networking for e-health applications," *Wireless Communications, IEEE*, vol. 20, no. 4, pp. 74–81, 2013.
- [8] —, "Medium access control and rate adaptation for ultrasonic intra-body sensor networks," *IEEE/ACM Transactions on Networking*, 2014.
- [9] T. Melodia, H. Kulhandjian, L. Kuo, and E. Demirors, "Advances in Underwater Acoustic Networking," in *Mobile Ad Hoc Networking: Cutting Edge Directions*, second edition ed., S. Basagni, M. Conti, S. Giordano, and I. Stojmenovic, Eds. Inc., Hoboken, NJ: John Wiley and Sons, 2013, pp. 804–852.
- [10] T. Dahl, J. L. Ealo, H. J. Bang, S. Holm, and P. Khuri-Yakub, "Applications of airborne ultrasound in human-computer interaction," *Ultrasonics*, vol. 54, no. 7, pp. 1912 – 1921, 2014.
- [11] P. Lazik and A. Rowe, "Indoor pseudo-ranging of mobile devices using ultrasonic chirps," in *Proc. of the ACM Conf. on Embedded Network Sensor Systems*, 2012.
- [12] G. Oberholzer, P. Sommer, and R. Wattenhofer, "Spiderbat: Augmenting wireless sensor networks with distance and angle information," in *Proc. of Intl. Conf. on Information Processing in Sensor Networks (IPSN)*, Apr. 2011.
- [13] R. Przybyla, H.-Y. Tang, S. Shelton, D. Horsley, and B. Boser, "3D ultrasonic gesture recognition," in *Proc of IEEE Intl. Solid-State Circuits Conference Digest of Technical Papers (ISSCC)*, Feb. 2014.
- [14] F.L. Thurstone, H.E. Melton, "Biomedical Ultrasonics," *IEEE Trans. on Ind. Electr. and Contr. Instrum.*, vol. 17, no. 2, Apr. 1970.
- [15] D. Kurup, W. Joseph, G. Vermeeren, and L. Martens, "Path loss model for in-body communication in homogeneous human muscle tissue," *Electronics Letters*, vol. 45, no. 9, pp. 453–454, 2009.
- [16] K. Sayrafian-Pour, W.-B. Yang, J. Hagedorn, J. Terrill, and K. Yazdandoost, "A statistical path loss model for medical implant communication channels," in *Personal, Indoor and Mobile Radio Communications, 2009 IEEE 20th International Symposium on*, 2009, pp. 2995–2999.
- [17] G. Lockwood, D. Turnball, D. Christopher, and F. Foster, "Beyond 30 MHz [applications of high-frequency ultrasound imaging]," *IEEE Engineering in Medicine and Biology Magazine*, vol. 15, no. 6, Nov/Dec 1996.
- [18] R. Smith, A. Arca, X. Chen, L. Marques, M. Clark, J. Aylott, and M. Somekh, "Design and fabrication of nanoscale ultrasonic transducers," *Journal of Physics: Conference Series*, vol. 353, no. 1, 2012.
- [19] A. Y. Cheung and A. Neyzari, "Deep local hyperthermia for cancer therapy: External electromagnetic and ultrasound techniques," *Cancer Res. (Suppl.)*, vol. 44, no. 9, 1984.
- [20] T. Hogg and R. A. Freitas, "Acoustic Communication for Medical Nanorobots," *Nano Communication Networks (Elsevier)*, vol. 3, no. 2, pp. 83–102, Feb. 2012.
- [21] U.S. Food Drug Administration (FDA), "Information for manufacturers seeking marketing clearance of diagnostic ultrasound systems and transducers," 2008. [Online]. Available: <http://goo.gl/ErZ19g>
- [22] IEEE Standard Association, "802.15.6-2012 - IEEE standard for local and metropolitan area networks - part 15.6: Wireless body area networks," 2012.
- [23] R. Chávez-Santiago, I. Balasingham, and J. Bergsland, "Ultrawideband technology in medicine: a survey," *Journal of Electrical and Computer Engineering*, vol. 2012, pp. 3:1–3:9, 2012.
- [24] M. M. Lee, E.-M. Lee, B. L. Cho, K. Eshraghian, and Y.-H. Kim, "The UTCOMS: a wireless video capsule nanoendoscope," in *Proc. of SPIE*, vol. 6082, 2006, pp. 60 820F–60 820F–10.
- [25] K. Zhang, Q. Hao, Y. Song, J. Wang, R. Huang, and Y. Liu, "Modeling and characterization of the implant intra-body communication based on capacitive coupling using a transfer function method," *Sensors*, vol. 14, no. 1, p. 1740, 2014.
- [26] M. Swaminathan, F. Cabrera, J. Pujol, U. Muncuk, G. Schirner, and K. Chowdhury, "Multi-path model and sensitivity analysis for galvanic coupled intra-body communication through layered tissue," *Biomedical Circuits and Systems, IEEE Transactions on*, vol. PP, no. 99, pp. 1–1, 2015.
- [27] Y. Davilis, A. Kalis, and A. Ifantis, "On the use of ultrasonic waves as a communications medium in biosensor networks," *IEEE Transactions on Information Technology in Biomedicine*, vol. 14, no. 3, May 2010.
- [28] M. Peisino and P. Ryser, *Deeply Implanted Medical Device Based on a Novel Ultrasonic Telemetry Technology*. EPFL, 2013.
- [29] C. R. Hill, *Ultrasonic attenuation and scattering by tissues*. John Wiley & Sons, Inc., 1978.
- [30] F. P. Bolin, L. E. Preuss, R. C. Taylor, and R. J. Ference, "Refractive index of some mammalian tissues using a fiber optic cladding method," *Appl. Opt.*, vol. 28, no. 12, pp. 2297–2303, Jun 1989.
- [31] USRP: Universal Software Radio Peripheral, Last access: Aug 2016. [Online]. Available: <http://www.ettus.com/>
- [32] WARP: Wireless Open-Access Research Platform, Rice University, Last access: Aug 2016. [Online]. Available: <http://warpproject.org>
- [33] G. Nychis, T. Hottelier, Z. Yang, S. Seshan, and P. Steenkiste, "Enabling MAC protocol implementations on software-defined radios," in *Proc. of USENIX symposium on Networked systems design and implementation*, Boston, MA, 2009.
- [34] K. Chowdhury and T. Melodia, "Platforms and Testbeds for Experimental Evaluation of Cognitive Ad Hoc Networks," *IEEE Communications Magazine*, vol. 48, no. 9, pp. 96–104, Sep 2010.
- [35] GNU Radio - The GNU Software Radio, Last access: Aug 2016. [Online]. Available: <http://www.gnuradio.org>
- [36] Mini-Circuits: RF/IF & Microwave components DC to 40 GHz, Last access: Aug 2016. [Online]. Available: <http://www.minicircuits.com/>
- [37] K. Shung and M. Zippuro, "Ultrasonic transducers and arrays," *IEEE Engineering in Medicine and Biology Magazine*, vol. 15, no. 6, pp. 20–30, nov 1996.
- [38] The Ultran Group, Last access: Aug 2016. [Online]. Available: <http://www.ultrangroup.com>

- [39] M. O. Culjat, D. Goldenberg, P. Tewari, and R. S. Singh, "A review of tissue substitutes for ultrasound imaging," *Ultrasound in Medicine & Biology*, vol. 36, no. 6, pp. 861–873, 2010.
- [40] CIRS: Kidney Training Phantom, Last access: Aug 2016. [Online]. Available: <http://www.cirsinc.com/products>
- [41] K. Tan, H. Liu, J. Zhang, Y. Zhang, J. Fang, and G. M. Voelker, "Sora: high-performance software radio using general-purpose multi-core processors," *Commun. ACM*, vol. 54, no. 1, pp. 99–107, Jan. 2011.
- [42] M. Di Benedetto, *Ultra-wideband Communication Systems: A Comprehensive Overview*, ser. EURASIP Book Series on Signal Processing and Communications. Hindawi Publishing Corporation, May 2006.
- [43] Q. Huynh-Thu and M. Ghanbari, "Scope of validity of psnr in image/video quality assessment," *Electronics Letters*, vol. 44, no. 13, pp. 800–801, June 2008.
- [44] Z. Wang, A. Bovik, H. Sheikh, and E. Simoncelli, "Image quality assessment: from error visibility to structural similarity," *IEEE Transactions on Image Processing*, vol. 13, no. 4, pp. 600–612, April 2004.
- [45] "Tables of physical & chemical constants. 2.1.2 barometry, cpt. 2. sec 4.6," www.kayelaby.npl.co.uk, Tech. Rep., Last access: Aug 2016.
- [46] "Atlas of gastrointestinal video endoscopy," Last access: Aug 2016. [Online]. Available: <http://www.gastrointestinalatlas.com>
- [47] GStreamer, open source multimedia framework, Last access: Aug 2016. [Online]. Available: <http://gstreamer.freedesktop.org/>
- [48] EvalVid - A Video Quality Evaluation Tool-set, Last access: Aug 2016. [Online]. Available: <http://www.tkn.tu-berlin.de/menue/research/evalvid/>
- [49] T. F. Rappaport, *Wireless Communications: Principles and Practice*. Prentice-Hall, 1999.
- [50] P. M. Shankar, "A General Statistical Model for Ultrasonic Backscattering from Tissues," *IEEE Transactions on Ultrasonics, Ferroelectrics, and Frequency Control*, vol. 47, no. 3, May 2000.
- [51] P. Shankar, "Ultrasonic tissue characterization using a generalized nakagami model," *IEEE Transactions on Ultrasonics, Ferroelectrics and Frequency Control*, vol. 48, no. 6, pp. 1716–1720, 2001.
- [52] T. Eltoft, "Modeling the amplitude statistics of ultrasonic images," *IEEE Transactions on Medical Imaging*, vol. 25, no. 2, pp. 229–240, 2006.



G. Enrico Santagati (S'13) is a Ph.D. student with the Department of Electrical and Computer Engineering, Northeastern University, Boston, MA, USA. He is currently working with the Wireless Networks and Embedded Systems Laboratory under the guidance of Prof. Tommaso Melodia. He received the B.S. and M.S. degrees in telecommunication engineering from the University of Catania, Catania, Italy, in 2010 and 2012, respectively. His current research interests are in ultrasonic intra-body networks and software defined radios.



Tommaso Melodia (M'07) received the Ph.D. degree in electrical and computer engineering from the Georgia Institute of Technology, Atlanta, GA, USA, in 2007. He is an Associate Professor with the Department of Electrical and Computer Engineering, Northeastern University, Boston, MA, USA. His research has been supported by the National Science Foundation, Air Force Research Laboratory, and the Office of Naval Research, among others. His current research interests are in modeling, optimization, and experimental evaluation of networked communication systems, with applications to ultrasonic intra-body networks, cognitive and cooperative networks, multimedia sensor networks, and underwater networks.

Prof. Melodia was a recipient of the National Science Foundation CAREER Award and coauthored a paper that was recognized as the ISI Fast Breaking Paper in the field of Computer Science for February 2009 and of Best Paper Awards of ACM WUWNet 2013 and 2015. He was the Technical Program Committee Vice Chair for IEEE GLOBECOM 2013 and the Technical Program Committee Vice Chair for Information Systems for IEEE INFOCOM 2013. He serves on the editorial boards of the IEEE TRANSACTIONS ON MOBILE COMPUTING, the IEEE TRANSACTIONS ON WIRELESS COMMUNICATIONS, the IEEE TRANSACTIONS ON MULTIMEDIA, and Computer Networks.